Test of the diffusing-diffusivity mechanism using near-wall colloidal dynamics

Mpumelelo Matse,[1] Mykyta V. Chubynsky,[2,*] and John Bechhoefer[1,†]
[1]*Department of Physics, Simon Fraser University, Burnaby, British Columbia, Canada V5A 1S6*
[2]*Department of Physics, University of Ottawa, 150 Louis-Pasteur, Ottawa, Ontario, Canada K1N 6N5*
(Received 23 February 2016; revised manuscript received 3 June 2017; published 11 October 2017)

The mechanism of diffusing diffusivity predicts that, in environments where the diffusivity changes gradually, the displacement distribution becomes non-Gaussian, even though the mean-square displacement grows linearly with time. Here, we report single-particle tracking measurements of the diffusion of colloidal spheres near a planar substrate. Because the local effective diffusivity is known, we have been able to carry out a direct test of this mechanism for diffusion in inhomogeneous media.

DOI: 10.1103/PhysRevE.96.042604

I. INTRODUCTION

The simple picture of Brownian motion due to Einstein, von Smoluchowski, and others [1–3] leads to stochastic motion where the mean-square displacement (MSD) is linear in time t and where displacements are Gaussian distributed. This picture, appropriate for an isolated object diffusing in a homogeneous and infinite medium, breaks down in more complex environments. For example, in some situations, the motion of molecules that diffuse inside the crowded environment of a cell has been described by anomalous diffusion, with a MSD having sublinear behavior $\sim t^{\alpha}$, with $0 < \alpha < 1$ [4–8]. In some cases (described by the fractional-Brownian-motion model), the accompanying displacement distributions remain Gaussian [9], while in others (continuous-time-random-walk model) they are non-Gaussian [10,11].

Another group of experiments has also reported deviations from simple Brownian motion in complex media, with MSDs that are linear but with displacement distributions having tails that decay more slowly than Gaussian. Such *non-Gaussian yet normal* diffusion has been reported on lipid tubules and in networks of filamentous molecules [12,13], polymer systems [14–16], porous media [17], active-matter systems [18,19], supercooled liquids [20,21], and colloidal suspensions [22], as well as in simulations of two-dimensional (2D) disks [23] and porous media [24]. This behavior is believed to arise in complex environments where the effective diffusion constant varies in space, or time, or both. The picture is that the observed motion is the superposition of ordinary diffusion processes that, over short time intervals, are simple, with Gaussian displacements characterized by some local diffusion constant. Displacement distributions for an ensemble of particles then convolute the contribution of Gaussian distributions with different variances, generally leading to an overall non-Gaussian distribution. For longer time intervals, the central limit theorem ensures that displacements are Gaussian. By contrast, the MSD increases linearly as a function of the time interval, as for normal diffusion. This picture, developed qualitatively in Refs. [12,13] and explained theoretically in Ref. [25], has inspired much theoretical investigation [26–31].

In the experiments done to date, the characteristics of the complex environment, such as the local value of D, were not measured independently and were known at best statistically [12–16,18–24]. Here, we report experimental observations of single-particle diffusion in a system where the underlying D variations are known independently. Knowing explicitly the variations in D, we then carry out a direct test of the diffusing-diffusivity mechanism proposed in Ref. [25] to account for non-Gaussian yet normal diffusion.

Below, in Sec. II, we describe the experimental apparatus and associated procedures for data collection and processing. In Sec. III, we discuss the variation of diffusion constant with height above the substrate, the form of the vertical confining potential, and the use of kurtosis to quantify non-Gaussianity in a distribution. Then, in Sec. IV, we present our main results showing non-Gaussian displacements due to diffusing diffusivity in vertical motions. In Sec. V, we present computer simulations of particle motion that confirm that non-Gaussian displacements for short time intervals are due to variations in the diffusivity. We also use simulations to estimate uncertainties in various measured parameters. In Appendix A, we show that non-Gaussian effects are too small to be seen in horizontal displacements. Finally, we discuss how to estimate the kurtosis without bias (Appendix B) and give a simple estimate of the "critical" time interval beyond which confinement effects (specific to our experimental situation and not taken into account by the diffusing-diffusivity model) are significant (Appendix C).

II. EXPERIMENTAL BACKGROUND

A. Setup

In our experimental setup, a home-built bright-field microscope was used to image beads in three dimensions in reflection (Fig. 1). A halogen bulb fiber-optic illumination [32] was used as a light source, made more uniform by putting a ground-glass plate in front of it. We used a 60× water-immersion objective [33].

Samples were prepared as follows: Latex spheres were diluted and mixed with purified water, at volume fractions low enough that each bead can be considered to move independently from all others. Sample chambers (≈60–80 μm in thickness) were made by placing four pieces of Parafilm® [34] between a microscope slide (1 mm thick) and a no. 1

*Present address: Mathematics Institute, University of Warwick, Coventry CV4 7AL, United Kingdom.
†johnb@sfu.ca

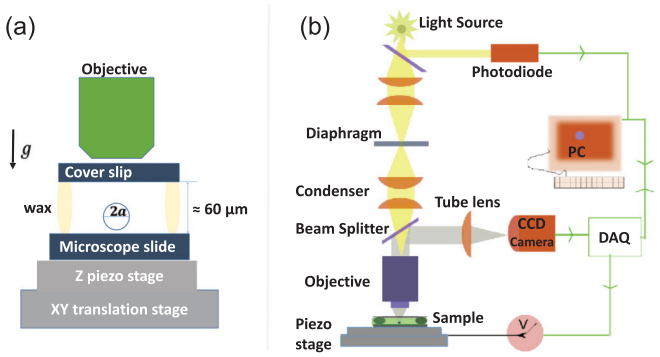

FIG. 1. Schematic diagram of experimental setup. (a) Details of sample. (b) Microscope and feedback loop used to track the beads.

coverslip (≈0.17 mm thick). The coverslip was first cleaned using a nitrogen gas ionizing gun [35] before use. The cell was partially sealed using Parafilm melted on a hot plate, then filled (without bubbles) with the beads in solution. Finally, the cell was completely sealed with melted wax in order to avoid fluid flow due to evaporation or convection and allowed to cool. The sample was then placed on an XY translation stage [36], which moved the sample to search for beads. A feedback-controlled piezostage [37] was used for tracking the z positions of the beads.

To eliminate mechanical drift due to thermal expansion or contraction between the sample cell and the microscope objective, we also tracked an immobilized bead (stuck to the substrate) as a reference from which the height z of the diffusing bead above the substrate could be determined using a fit of the intensity profile. We set the objective-stage separation to be just out of focus, so that the intensity of the two beads was located on the right side of the profile (Fig. 2). This ensured that none of the beads had positions on the other side of the profile, which would lead to ambiguity in the bead's position, as the profile is almost symmetric at the peak. We then applied a feedback loop to stabilize the position of the stuck bead.

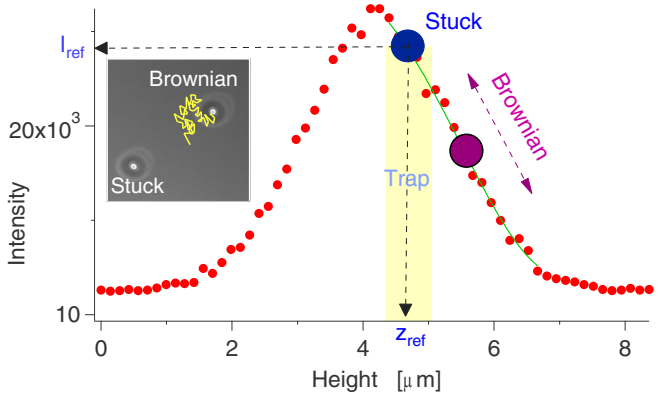

FIG. 2. Intensity profile of the central region of a bead stuck to the microscope slide. The stuck bead was kept at height z_{ref} by a feedback loop, while the Brownian bead diffused above the stuck bead. Inset shows camera image of both stuck and Brownian (freely diffusing) beads. The thin green line indicates the extent of the linear region of the intensity curve.

By choosing larger beads ($r \approx 2.5$ μm), we ensured that the maximum height of the diffusing bead was always within the linear regime depicted by the thin green line in Fig. 2. The differential measurement also eliminates noise due to variation of the light source.

Images were recorded by a CCD camera [38]. The image acquired was processed via the computer, using LABVIEW software [39], to determine the position of the bead. The camera was triggered by the rising edge of a square wave from a function generator [40]. The camera's frame rate was set to 30 Hz and the shutter speed to $t_{expt} = 10$ ms. Intensities were digitized at 12-bit resolution ($2^{12} = 4096$) and mapped onto a 16-bit intensity scale ($2^{16} = 65\,536$). The field of view of the camera was about 60 μm × 40 μm.

B. Position measurement of the bead

We acquired and processed images at fixed time intervals (33 ms) to determine the bead's trajectory. If the monitored bead diffused out of the field of view, we used the XY stage to manually reset the bead's image to the center of the field of view and continued collecting data on the same bead. In practice, we could obtain trajectories up to about 10^4 s. As described in the following two sections, separate algorithms were used to determine the horizontal and vertical positions of the bead.

The horizontal position was obtained using the edge-detecting algorithm from the IMAQ Vision module for LABVIEW, which locates a circular edge in a defined search area. The algorithm detects intersection points between a set of search lines defined by a spoke and the edge of an object. The intersection points are mainly determined based on the contrast in the image. This method works by first making an initial guess for the location of the bead. Next, any background intensity below some intensity threshold is set to zero, in order not to bias the center-of-mass calculation. Finally, a local region around the initial guess is selected and the center of mass used to estimate the bead center. The pixel coordinates of the bead's center of mass were then converted to microns. To calibrate distances, we imaged a 2D grating with 5×5 μm^2 grid squares. As determined from a stuck bead, horizontal position measurements were Gaussian distributed, with a standard deviation that was typically 6 nm.

The bead's vertical position was inferred directly from intensity images by averaging pixel intensities over a 3×3 pixel region centered on the pixel with the maximum intensity. The size of this region is *smaller* than the bead size (roughly 10×10 pixels) in order to increase the sensitivity of the (partial) intensity measurement to vertical displacements, while still maintaining adequate position resolution. The bead's intensity profile against height relative to the objective (Fig. 2) was obtained by vertically moving an immobilized bead, using a voltage applied to a calibrated piezostage and measuring the intensity of the bead from the images taken. An intensity calibration was performed before and after each set of measurements. Vertical position measurements were Gaussian distributed, with a standard deviation that was typically 12 nm.

To correct for uneven illumination, which could bias our height measurements of the Brownian bead, we normalized the bead intensity pixel by pixel, using the intensity of an

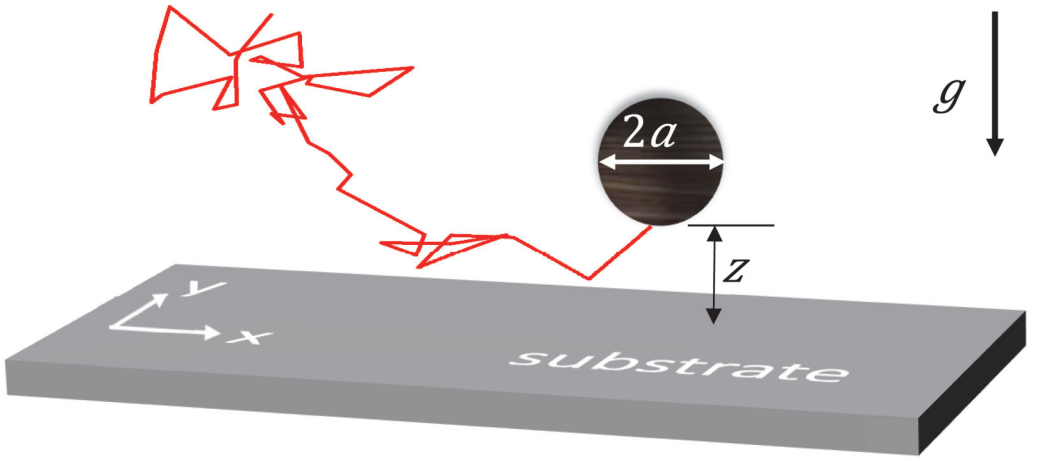

FIG. 3. Brownian diffusion near a horizontal substrate. Sphere of diameter $2a$ diffuses a height z above the surface, in a vertical gravity field g.

averaged background image. This procedure was done before and then checked after the Brownian bead measurements were taken, to ensure that the background image stayed uniform throughout the experiment. We redid experiments where any significant change was detected. The bead's intensity values were further normalized by the illumination intensity recorded by a photodiode. We eliminated the effects of stray ambient light by covering the microscope with a box.

To counter thermal and mechanical drifts that altered the distance between the objective and the sample, a feedback loop was used, as follows: For each image taken, a LABVIEW program determines the stuck bead's intensity I. The slope b from a linear fit is used to calculate a required voltage $V = \alpha(I - I_{\rm ref})/b$, where α is the feedback gain, to move the stuck bead back to the set plane (at $I_{\rm ref}$). Using a National Instruments data acquisition device (NI-USB 6215), the voltage is applied, and the iteration continues.

C. Estimating the diffusion constant at one height

In order to estimate the variation of the diffusion constant with the height z above the substrate, we measured displacements Δx and Δz conditioned on starting in a given height interval of width $\Delta z_{\rm bin}$. That is, $z \in (z_{{\rm bin}n}, z_{{\rm bin}n} + \Delta z_{\rm bin})$. Denoting the mean-square conditional vertical displacement by

$$\langle(\Delta z)^2\rangle_n, \tag{1}$$

the estimate of $D_{\rm perp}(z)$ for bin n is

$$D_{\rm perp}(z)_n = \frac{\langle(\Delta z)^2\rangle_n - 2\xi^2)}{2\left(\Delta t - \frac{1}{3}t_{\rm expt}\right)}, \tag{2}$$

where the denominator corrects for the blurring effects of the camera exposure, and $t_{\rm expt} = 10$ ms, which is not small compared to the measurement interval $\Delta t = 33$ ms. The ξ^2 term represents the variance of the measurement noise (assumed uncorrelated and identically distributed at different times), which is estimated as $\xi \approx 0.004$ μm by extrapolating the autocorrelation function of position measurements as a function of shift and isolating the "extra" variance at zero shift. See Refs. [41–43] for derivation and discussion of the motion-blur effect. Since the measurement noise in the time series for z was quite small, it had negligible effect on the diffusion-constant estimates.

III. THEORETICAL BACKGROUND

A. Variation of diffusion constant with height

For our experiments, we consider the Brownian motion of a colloidal sphere near a planar horizontal surface (Fig. 3), a situation where the diffusion constant varies in a known way with distance from the surface. For a freely diffusing Brownian sphere in an unbounded fluid medium, the diffusivity is given by the Stokes-Einstein relation, $D_0 = \frac{k_B T}{6\pi\eta a}$, where k_B is Boltzmann's constant, T the temperature, a the particle radius, and η the fluid's dynamic viscosity. For diffusion near a solid planar surface, theoretical [44–46] and experimental [47–53] studies have shown that the diffusivity decreases anisotropically with distance z from the plane, owing to the hydrodynamic interaction between the sphere and the plane. A useful second-order Padé approximation [47] to the infinite-series results found by Brenner [46] gives the vertical diffusivity to within 1% accuracy,

$$D_\perp(z) \cong D_0\left(\frac{6z^2 + 2az}{6z^2 + 9az + 2a^2}\right), \tag{3}$$

where z is the height of the bead bottom above the substrate (Fig. 3). For small z, we have $D_\perp/D_0 \approx z/a$.

By contrast, for small z, the value of $D_\parallel$ is significantly higher and its relative variation much smaller (except perhaps extremely close to the plane [46]). As we will see, the stronger relative variation of $D_\perp$ can lead to non-Gaussian dynamics, whereas the weaker relative variation in $D_\parallel$ does not generate measurable deviations from Gaussian displacement distributions (Appendix A). The experiments presented below consider vertical motion only.

B. Particle potential variation with height

Near a horizontal substrate, the vertical motion of a sphere is influenced by both gravitational and electrostatic forces. The surface of the colloidal particle and the substrate in a liquid may carry ionized chemical groups, which in our experiments lead to repulsive electrostatic double-layer forces that prevent the Brownian particles from sticking to each other and to the surface of the substrate [54]. For large-enough heights, van der Waals forces can be neglected since they are very short ranged (order of a few nanometers) and are masked by the longer-ranged double-layer forces (50–100 nm). The total potential energy $U(z)$ of a diffusing particle is therefore dominated by the gravitational field at larger heights and the double-layer potential at smaller heights:

$$\frac{U(z)}{k_BT} = \begin{cases} \bar{B}e^{-z/\ell_D} + z/\ell_g, & z \geqslant 0 \\ \infty, & z < 0, \end{cases} \tag{4}$$

where ℓ_D is the *Debye length*, which measures the effectiveness of the screening—the range of double-layer interaction effects. In experiments, we chose a Debye length large enough to keep the sphere-substrate interactions simple by eliminating van der Waals forces. The prefactor $\bar{B}$ measures the strength of the double-layer potential, in units of k_BT. The *gravitational decay length* $\ell_g = \frac{k_BT}{\Delta mg}$ is the length defined by equating the gravitational potential energy to k_BT. Also, $\Delta m = \Delta\rho(\frac{4}{3}\pi a^3)$ is the mass difference between particle and displaced solvent, and $\Delta\rho$ is the corresponding density difference.

Given the potential (4), the motion of the particle is described by the overdamped Langevin equation, according to which its displacement in a short interval δt is given by [55,56] (cf. Appendix C)

$$\Delta z \approx \left[\frac{dD_\perp(z)}{dz} - \frac{D_\perp(z)}{k_BT}\frac{dU(z)}{dz}\right]\delta t + \sqrt{2D_\perp(z)\delta t}\,\xi, \tag{5}$$

where we use the *isothermal rule* for stochastic integration [55,57]. Here, ξ is a Gaussian random variable satisfying $\langle\xi\rangle = 0$ and $\langle\xi^2\rangle = 1$.

Apart from the above-mentioned three length parameters—a, ℓ_D, and ℓ_g—that can be controlled in experiments, the time interval Δt over which the displacements are measured is important. To observe the diffusing-diffusivity mechanism, we need to ensure that variations in D are the dominant contribution to non-Gaussian dynamics within Δt. Since the bounding potential can lead to undesired nonlinear MSD, along with non-Gaussian dynamics, we work in a regime where thermal fluctuations dominate over deterministic drift. As discussed in Appendix C, for diffusion to dominate, we impose $\overline{\Delta t} \equiv \Delta t(D_0/\ell_g^2) < \overline{\Delta t}_c$. A simple estimate based on a harmonic approximation to the potential of Eq. (4) then predicts $\overline{\Delta t}_c \approx 12$ for the parameters typical of our experiment.

Another requirement is that the experimental parameters should lead to non-Gaussian displacement distributions. If, for example, the bead size is too small, then the gravitational length will be too large and relative variations in D too small to generate significant deviations from a Gaussian distribution. Thus, we chose parameters carefully so that the value of ℓ_g/a is small—but not so small that the statistical errors of height measurement dominated.

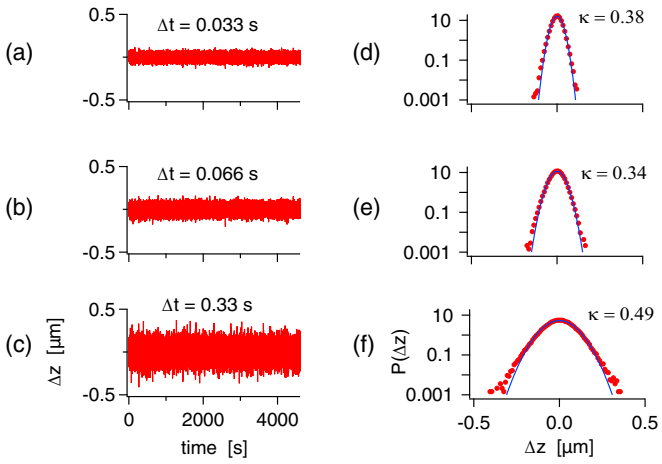

FIG. 4. (a)–(c) Time series of vertical displacements and (d)–(f) histograms. Data from run 10.

To measure the deviations from a Gaussian distribution, we used the *excess kurtosis* statistic,

$$\kappa \equiv \frac{\langle\Delta z^4\rangle}{[\langle\Delta z^2\rangle]^2} - 3, \tag{6}$$

which is defined so that $\kappa = 0$ for a Gaussian distribution and $\kappa > 0$ for a heavier-tailed distribution [58]. We found that latex beads of radius 2.5 μm in purified water above a glass substrate gave an easily measurable diffusing-diffusivity effect for vertical motion.

IV. RESULTS

In this section, we present the results of different experiments on vertical displacements to test the proposed mechanism of diffusing diffusivity presented by Ref. [25]. In Sec. IV A, we show that vertical displacements of a long time series show evidence for non-Gaussian distributions using both histograms and the excess-kurtosis statistic. In Sec. IV B, we generate histograms of height measurements and fit them with the Boltzmann distributions, from which we estimate potential and material parameters. Then, in Sec. IV C, we study the excess kurtosis and mean-square displacement as a function of the time interval. The challenge is to separate out the non-Gaussian effects arising due to varying diffusion "constant" from effects due to the confinement by the vertical potential (balance of electrostatic and gravitational forces).

A. Vertical displacements

Figure 4 shows time series and vertical displacements for three different time intervals. The slight deviation in the tails from a Gaussian distribution leads to a positive excess kurtosis.

B. Height distributions and parameter determination

The distribution of heights for one bead trajectory is shown in Fig. 5(a). The solid line is the least-squares fit to the Boltzmann distribution $P_B(z) \propto \exp[-U(z)/k_BT]$, using Eq. (4). The fit parameters were $\ell_g = 0.113 \pm 0.005$ μm (expected value using nominal bead size from manufacturer

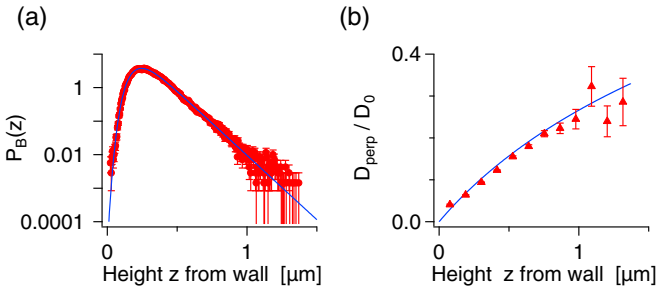

FIG. 5. (a) Probability density function $P_B(z)$ of bead height above substrate, z. Solid line is a fit to the Boltzmann distribution, Eq. (4). (b) Vertical diffusivity of the bead vs z. Solid line is a plot—not fit—of Eq. (3), using material parameters inferred from (a). Data from run 10, with parameters from Table I.

of $\approx 0.11 \pm 0.02$ μm), $\ell_D = 0.079 \pm 0.004$ μm, and $\bar{B} = 15.3 \pm 0.8$ (Sec. II A). The height reference $z_{\rm ref}$ (substrate position) is also fit. Since ℓ_g is well determined from the data, we used it to infer the bead size. For the data in Fig. 5(a), we find $a = 2.53 \pm 0.04$ μm. The variation of the bead's vertical diffusivity with height from the substrate is shown in Fig. 5(b). The diffusion coefficients are measured using conditional displacements Δz in a narrow interval (0.1 μm) centered on height z above the substrate, correcting for the camera exposure $t_{\rm expt}$ by means of Eq. (2). Using the asymptotic diffusivity $D_0 = 0.0996 \pm 0.0015$ μm^2/s calculated from the inferred parameters, we plot the normalized diffusivity $D_\perp(z)/D_0$ from Eq. (3) in Fig. 5(b), with no adjustable parameters.

For Fig. 6, we collected 13 sets of data for different trajectories averaging about 45 min (82 000 data points) each. The results are summarized in Table I.

A histogram estimate of the position probability density for each run was fit separately to the Boltzmann distribution to obtain 13 sets of the parameters ℓ_g, ℓ_D, and B [59]; the values of a and D_0 were then obtained from ℓ_g. For these histograms, a bin width of 5 nm was chosen, which is sufficiently small that the probability density does not change significantly over that length. A weighted least-squares fitting procedure was used, with the weights inversely proportional to the number of data points in the bin and the bins with zero points ignored. Because of correlations between bins, we used simulations to estimate parameter uncertainties. We thereby estimated the uncertainties for ℓ_g, ℓ_D, and $\bar{B}$ as 5 nm, 4 nm, and 0.8, respectively, for the longest runs and 10 nm, 8 nm, and 1.7 for the shortest runs. The corresponding uncertainty of a is 35–70 nm, while for D_0 it is 0.0015–0.003 μm^2/s. See Sec. V for details on the simulation methods.

The resulting sets of parameters are given in Table I. We see that the values are consistent with expected bead-to-bead variations and with theory expectations. The amount of variation seen in the radius ($\approx \pm 2\%$) inferred in different runs is typical of manufacturer specifications for the coefficient of variation of the diameter.

Finally, we mention an important point in our analysis. Consider an imaginary series of runs using the same bead under the same conditions. We refer to the run-to-run variations of estimates of various quantities in such a series as their statis-

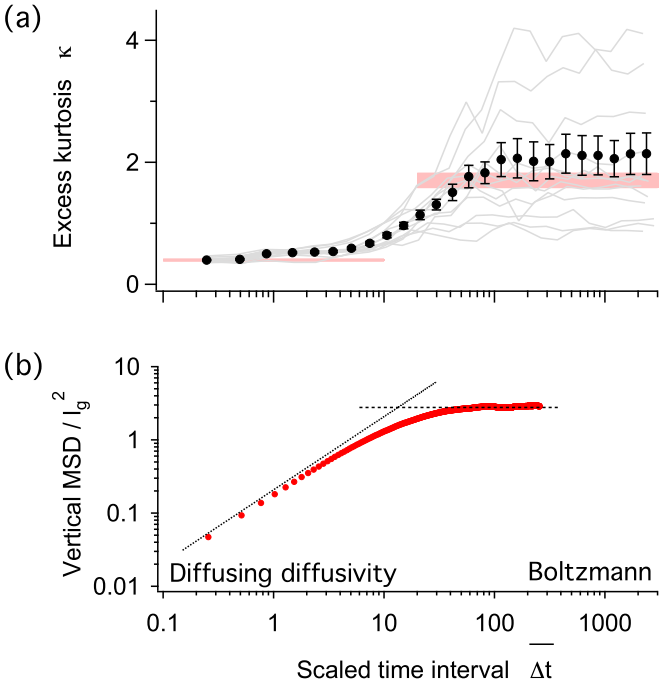

FIG. 6. Diffusing diffusivity and Boltzmann regimes for short and long time intervals, with $\overline{\Delta t} = \Delta t(D_0/\ell_g^2)$. (a) Excess kurtosis is nonzero for all intervals. Light gray curves show results from 13 individual runs (Table I). Solid symbols represent the unbiased estimate based on the 13 runs, with the standard error of this estimate shown, too. Uncertainties in the scaled time interval $\overline{\Delta t}$ are $\approx 2\%$, which is smaller than the symbol size. Pink bars represent the diffusing-diffusivity limit at short time intervals and the Boltzmann limit at long time intervals. (b) Mean-square displacement (MSD). Data from run 10. Dotted line shows linear MSD behavior for short time intervals, with the slope obtained theoretically using parameters from Table I. Dashed line shows MSD for the difference between two position measurements drawn from the Boltzmann distribution for $U(z)$, as described by Eq. (8).

TABLE I. Values obtained for experimental parameters from 13 different runs. N gives the number of data points in the run. The radius a is inferred from ℓ_g using the measured temperature $T = 298.5 \pm 1$ K and latex bead density $\rho_b = 1.055$ g/cc. The D_0 values also use the water viscosity $\eta = (0.88 \pm 0.02) \times 10^{-3}$ N s/m^2.

Run	N	l_g (μm)	l_D (μm)	$\frac{B}{k_BT}$	a (μm)	D_0 (μm^2/s)
1	68 966	0.120	0.071	16.8	2.48	0.102
2	71 628	0.118	0.077	15.6	2.49	0.101
3	100 394	0.117	0.071	17.7	2.50	0.101
4	119 155	0.121	0.078	14.7	2.47	0.102
5	93 778	0.117	0.075	16.3	2.50	0.101
6	62 869	0.114	0.070	17.0	2.52	0.100
7	38 763	0.121	0.073	15.8	2.47	0.102
8	34 892	0.105	0.086	14.5	2.59	0.097
9	80 065	0.117	0.074	16.2	2.50	0.101
10	139 716	0.113	0.079	15.3	2.53	0.100
11	119 645	0.123	0.072	16.8	2.46	0.102
12	82 324	0.118	0.072	15.6	2.49	0.101
13	54 923	0.106	0.079	16.4	2.58	0.098

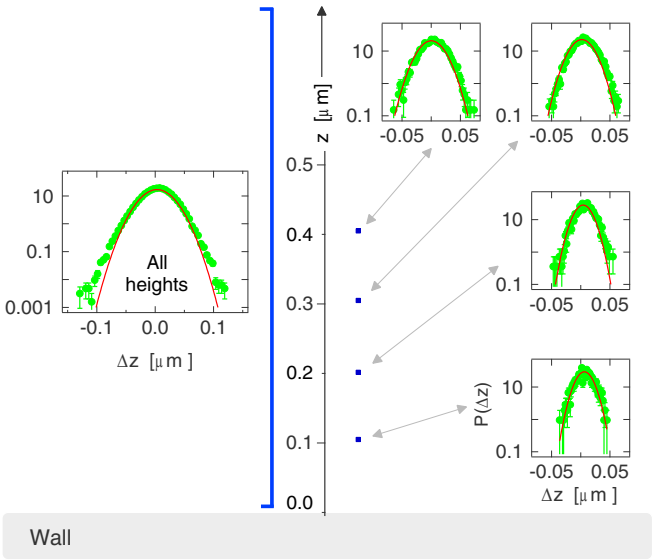

FIG. 7. Displacements at starting-point intervals of ≈0.01 μm close to the substrate. Right: The nearly Gaussian height conditional distributions. Left: The non-Gaussian distribution from all heights explored by the bead. $\Delta t = 0.033$ s. Data from run 10.

tical fluctuations. For quantities such as the bead radius a or asymptotic diffusion constant D_0 these statistical fluctuations are smaller than or comparable to the bead-to-bead variations of the true values of these quantities in the 13 actual runs we analyze. However, they are *larger* in the case of the excess kurtosis κ, where large statistical fluctuations arise because κ depends on the fourth moment of the probability distribution. Consequently, it makes sense to report a single estimate of κ based on the 13 runs. A proper way to obtain this estimate is described below. But for the MSD, which depends on only the second moment, and for the relation between diffusivity and height, one should look at the data from a single run.

C. Influence of the time interval

The excess kurtosis and MSD at different time scales are shown in Fig. 6. For the excess kurtosis, the results of 13 different runs are in light gray, and the unbiased estimate obtained from them as described in Appendix C is given by the solid symbols. To reduce statistical noise in the kurtosis, the data are binned, with the bin widths roughly constant on the logarithmic scale and data within each bin are averaged (or, rather, the same unbiased estimate procedure is applied) and assigned to the value of $\overline{\Delta t}$ corresponding to the average between the values within the bin. The displacements are non-Gaussian at all time scales, with heavier, nearly exponential tails, as illustrated by the histogram at left in Fig. 7 and also in Fig. 4. The excess kurtosis interpolates between ≈1.9 at large time intervals $\overline{\Delta t}$ to ≈0.4 at small time intervals, with a crossover at $\overline{\Delta t}_c \approx 20$, which is close to the value calculated theoretically (Appendix C). We notice that for each run the fluctuations for different values of $\overline{\Delta t}$ are correlated, because each point on a single curve is calculated from the same time series.

The two observed plateaus in kurtosis suggest that there are two regimes: diffusing diffusivity ($\Delta t < \Delta t_c$) and Boltzmann ($\Delta t > \Delta t_c$). In the diffusing-diffusivity regime, the non-Gaussian dynamics is driven by D variations, and the bounding potential has negligible influence. In this regime, the displacements are non-Gaussian; yet the MSD grows linearly with time [Fig. 6(b)]. The non-Gaussian displacement distribution is generated by the diffusivity distribution $P(D)$. Then, for $\Delta t \to 0$ [12,60],

$$P(\Delta z;\Delta t) \approx \int_0^\infty dD\, P(D)\, \frac{1}{\sqrt{4\pi D \Delta t}} \exp\left[-\frac{\Delta z^2}{4D\Delta t}\right]. \tag{7}$$

In Fig. 6(a), we see that the kurtosis is constant near the minimum time scales probed in the experiment. At these short time scales, $P(\Delta z)$ is governed chiefly by the time-independent $P(D)$. If D did not vary, we would expect no kurtosis (as observed for horizontal displacements; see Appendix A).

In the Boltzmann regime, the bounding potential dominates the D variations, and the MSD saturates [Fig. 6(b)]. At very large time intervals, we can view each position measurement as an independent sample from the equilibrium Boltzmann distribution. For $\Delta t \to \infty$,

$$P(\Delta z) \approx \int_{-\infty}^{\infty} dz\, P_B(z)\, P_B(z+\Delta z), \tag{8}$$

where the potential $U(z)$ in Eq. (4) and hence the Boltzmann distribution $P_B(z)$ is formally defined for all z, with $P_B(z) = 0$ for $z < 0$.

For the bounding potential in the system we study, Eq. (8) is clearly non-Gaussian (it has exponential tails $\propto e^{-|\Delta z|/\ell_g}$). The predicted values of the excess kurtosis for the 13 experimental runs based on the parameter estimates for these runs (see Table I) range from 1.42 to 1.82, with the average 1.70. The range is consistent with the unbiased estimate at large time intervals based on the 13 runs (Fig. 6), keeping in mind the small number of runs and the approximations made when estimating the uncertainties. The large spread between the runs for large Δt is mostly due to lack of statistics and is consistent with the results of numerical simulations, as discussed in Sec. V.

Finally, we divided the vertical-position measurements of the bead into very small height intervals (≈0.01 μm) in the diffusing-diffusivity regime ($\Delta t = 0.033$ s) and studied the displacement distribution in each interval (Fig. 7). The results directly confirm the diffusing-diffusivity mechanism predicted by Eq. (7): The displacements are nearly Gaussian at each interval with different variances (right side of Fig. 7); yet the overall distribution is non-Gaussian (left side of Fig. 7).

V. SIMULATIONS

To deepen our understanding of the experimental results, we carried out computer simulations of the motion of colloidal particles. Their main purpose is to confirm that taking into account the main physical factors (namely, the electrostatic and gravity forces and the variation in the diffusivity with the height above the substrate) is sufficient to match the experiments qualitatively and quantitatively, while neglecting the diffusivity variation leads to significant discrepancies with

the experimental results. We also used them to estimate parameter uncertainties, as described in Sec. IV.

To simulate the motion of the particles, we have used the Brownian dynamics approach. As in the experiments, 13 runs were carried out. Since we are interested in the evolution of the height z and the vertical motion is decoupled from the horizontal, a one-dimensional (1D) simulation is sufficient. At time $t = 0$ a particle starts at the height z drawn from the Boltzmann distribution corresponding to the potential of Eq. (4). Then at each simulation step z changes according to Eq. (5), with the time step $\delta t = 0.001$ s. The diffusivity varies with height according to Eq. (3). Since the experimental conditions vary little between the experimental runs, we have used the same parameters for all our runs, close to the average values in the experiment. Namely, $\ell_g = 0.116\ \mu$m, $\ell_D = 0.076\ \mu$m, $\bar{B} = 16$, $a = 2.51\ \mu m$, and $D_0 = 0.1\ \mu\text{m}^2/\text{s}$. Data for the z position were collected every 33 steps, or 0.033 s, the same interval as in the experiment. We have also done a series of runs emulating the "motion-blur" effect [see Eq. (2)], by averaging the position over 11 time steps. This has a very minor effect, which justifies neglecting this effect, e.g., when calculating the MSD and the excess kurtosis. These results are not presented here. Since one of our purposes is to verify that the significant discrepancies between different runs at large $\overline{\Delta t}$ seen in Fig. 6(a) are attributable to lack of statistics, we have used the same simulation durations as in the experimental run. For each run, the kurtosis of the displacement distribution was first calculated for time interval durations from 1 to 11 249 time steps of 0.033 s each; for each duration, the set of data used in the calculations consisted of the displacements over all the intervals of that duration (including overlapping ones) present in the run. To smooth the resulting kurtosis dependence, the data were binned, as in the experiments. The result is shown in Fig. 8(a), together with the unbiased estimate based on all 13 runs (solid circles with error bars). There is good agreement, both qualitative and quantitative, with the experimental results in Fig. 6.

We have also repeated the same simulations with one significant difference: the diffusivity was held constant and set equal to $D = 0.0104\ \mu\text{m}^2/\text{s}$, the value obtained by averaging Eq. (3) with the Boltzmann distribution. To facilitate the comparison with the variable-D case, the same seed value was used for the pseudorandom number generator in both cases. While the results [Fig. 8(b)] are similar for large $\overline{\Delta t}$, they are very different for small Δt, with the kurtosis in the constant-D case close to zero and significantly below the experimental values. The MSD dependencies are nearly identical in the two cases and similar to Fig. 6(b) (not shown).

A separate application of simulations was to estimate the uncertainties of the parameters, which is nontrivial because of correlations between the bins. We carried out two series of runs (400 runs in each) with identical parameters (same values close to the averages as quoted above). In one series, the lengths of all runs were as in the shortest experimental run (run 8), and in the other series, as in the longest run (run 10). For each of the 800 runs, the position distributions were obtained using the same bin width as for the experimental data and fitted with the Boltzmann distribution. For an infinitely long run, the fitting parameters would be identical to the simulation parameters, but for runs of a finite duration the distributions have random noise and so do the parameters of the fits. The standard deviations of these parameters are then used as the estimates of the uncertainties of the parameters in the experimental fits.

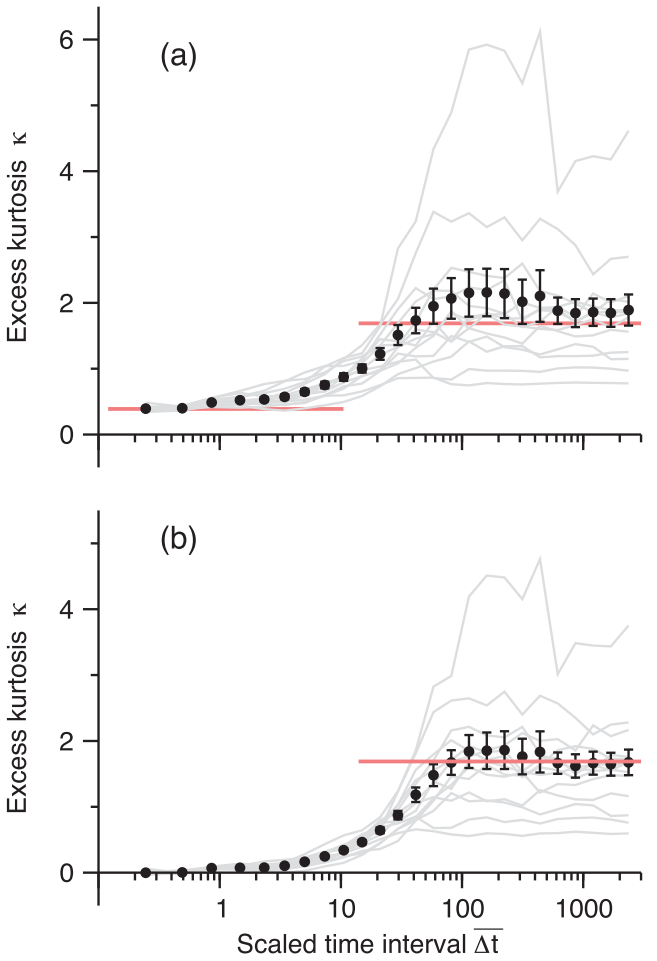

FIG. 8. Excess kurtosis of the vertical displacement distribution as a function of the time interval obtained in simulations, with the vertical diffusivity either (a) given by Eq. (3) or (b) constant and equal to the theoretical average. All other parameters roughly match the experimental conditions. The gray curves are the binned results for 13 individual realizations, and the solid circles with error bars are unbiased estimates based on these realizations. The horizontal red lines are the theoretical short- and long-time-interval limits. For details, see the text.

VI. CONCLUSION

In conclusion, we have investigated experimentally the Brownian motion of colloidal spheres near a planar surface and have made the first direct confirmation of the diffusing-diffusivity mechanism [25]: At small time intervals, non-Gaussian displacements coexist with a MSD that grows linearly with time. Our experimental system is unique among studies of this mechanism in that we independently measure the local value of the diffusivity, thereby showing that the conditional distributions starting within small height intervals from the substrate exhibit nearly Gaussian displacement distributions.

The results of the experiments reported here give a rigorous test of the diffusing-diffusivity mechanism in a model system with "quenched disorder" where diffusivity variations are measured independently. They suggest new ways to understand the behavior of other systems near walls and interfaces, such as the collective motion of sperm cells near interfaces [61] and swimming bacteria in thin films [62]. These quantitative results from a simple model system also give confidence in the more qualitative analyses done on more complex systems [12–14,17–22] where the same phenomena—linear MSD and non-Gaussian displacements—are observed.

ACKNOWLEDGMENTS

We thank Gary Slater and Maxime Ignacio for helpful discussions. We also thank Paul Omelchenko, Lukas Schertel, and Dirk Wiedmann for their contributions to the experimental apparatus. This work was supported by NSERC (Canada). M.V.C. also acknowledges support by Leverhulme Trust (United Kingdom) through a Research Project Grant to J. E. Sprittles.

APPENDIX A: MEASUREMENTS USING HORIZONTAL DISPLACEMENTS

We first attempted to study the bead's diffusing-diffusivity mechanism using horizontal displacements. Since there is no confining potential for horizontal motion, the diffusing-diffusivity mechanism does not compete with the effects linked to the potential. However, as we show in this Appendix, non-Gaussian effects for horizontal displacements are too small to measure, as the relative variation in D is significantly smaller than for vertical displacements.

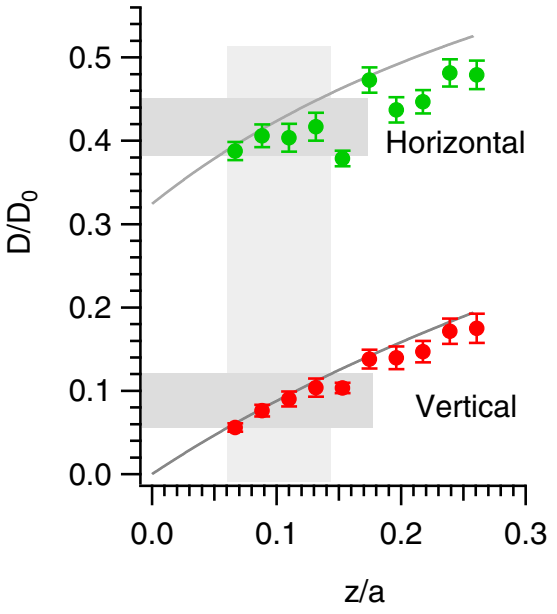

FIG. 9. Scaled horizontal and vertical diffusion coefficients, as a function of height z. Solid lines are plots—not fits—of Eqs. (1) and (A1), based on parameters from Table I. The shaded vertical strip depicts the typical range of heights explored, as estimated in Appendix C. Horizontal strips show corresponding diffusion constant variations. Data from run 10.

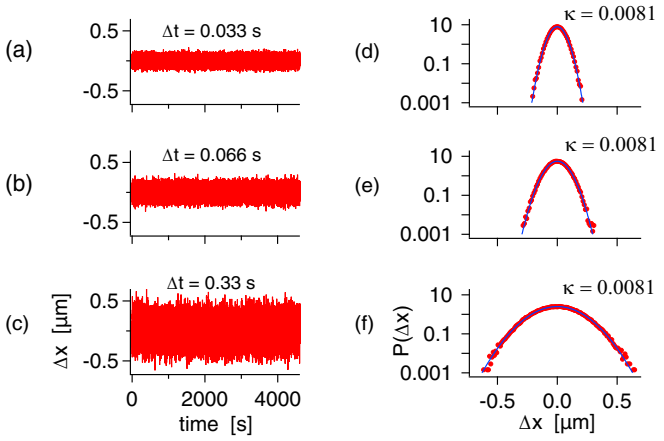

FIG. 10. (a)–(c) Time series of horizontal displacements and (d)–(f) histograms. Data from run 10.

Figure 9 compares the measured dimensionless horizontal and vertical diffusion coefficients, along with analytical estimates. The analytical estimate (solid line) for the vertical case is given by Eq. (3) and derived in Ref. [46]. Similarly, for the horizontal case, for sphere radius a and height above the substrate, z, we define $\delta \equiv \frac{a}{a+z}$. The horizontal variation in D is then

$$\frac{D_{\parallel}(z)}{D_0} = 1 - \frac{9}{16}\delta + \frac{1}{8}\delta^3 - \frac{45}{256}\delta^4 - \frac{1}{16}\delta^5 + O(\delta^6) \quad \text{(A1)}$$

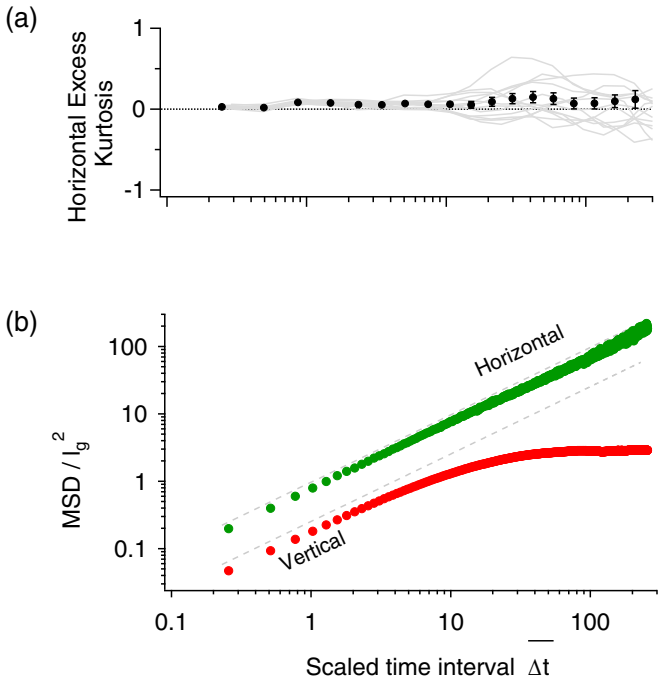

FIG. 11. Results for horizontal diffusion. (a) Excess kurtosis: individual runs (gray curves) and unbiased estimates (solid symbols with error bars). (b) MSD as a function of scaled time intervals $\overline{\Delta t} = \Delta t(D_0/\ell_g^2)$ for horizontal and vertical motions. Data from run 10.

for motion parallel to the substrate (e.g., along the x direction).

From the shaded strips in Fig. 9, we estimate the relative D fluctuations to be $\approx$0.08 for horizontal displacements and 0.33 for vertical displacements. As a result, relative $D_\parallel$ fluctuations are about four times smaller than their vertical counterparts, leading to a diffusing-diffusivity effect that was below our experimental resolution.

As we see in Fig. 10 and more systematically in Fig. 11, horizontal displacement distributions are nearly Gaussian. The excess kurtosis [Fig. 11(a)] is nearly zero for all times. The MSD remains linear with time [Fig. 11(b)] for all explored time intervals. Any trace of the diffusing-diffusivity mechanism is, unfortunately, too small to measure.

For more discussion of these results, see Ref. [63].

APPENDIX B: AN UNBIASED ESTIMATE OF THE EXCESS KURTOSIS

The ith moment of a random quantity ξ is defined as

$$m_i = \langle \xi^i \rangle. \tag{B1}$$

In practice, moments are estimated by taking a finite number N of samples from the distribution:

$$\widetilde{m_i} = \frac{1}{N}\sum_{j=1}^{N} \xi_j^i. \tag{B2}$$

The average of this estimate is

$$\langle \widetilde{m_i} \rangle = \left\langle \frac{1}{N}\sum_{j=1}^{N} \xi_j^i \right\rangle = \frac{1}{N}\sum_{j=1}^{N} \langle \xi_j^i \rangle = \frac{1}{N}\sum_{j=1}^{N} \langle \xi^i \rangle = m_i. \tag{B3}$$

This means that Eq. (B2) gives an *unbiased estimate* of the true value of the moment, m_i.

The situation is different for the excess kurtosis. Consider an estimate similar to Eq. (B2),

$$\begin{aligned}\overline{\kappa} &= \frac{1}{N}\sum_{j=1}^{N} \kappa_j = \frac{1}{N}\sum_{j=1}^{N} \frac{\widetilde{m_{4,j}}}{\widetilde{m_{2,j}}^2} - 3 \\ &= \frac{1}{N}\sum_{j=1}^{N} \frac{m_4 + \delta m_{4,j}}{(m_2 + \delta m_{2,j})^2} - 3,\end{aligned} \tag{B4}$$

where the deviations $\delta m_{i,j}$ of the measured moments $\widetilde{m_{i,j}}$ from their true values m_i are introduced. These measured moments are themselves calculated from a finite series of samples using Eq. (B2) (of course, generally speaking, with a different value of N, the number of samples), and since these are unbiased estimates, $\langle \delta m_{i,j} \rangle = 0$. Assuming for simplicity that these deviations are small and expanding in a Taylor series up to second order, we get

$$\begin{aligned}\overline{\kappa} \approx \frac{m_4}{(m_2)^2} &\times \frac{1}{N}\sum_{j=1}^{N}\left(1 + \frac{\delta m_{4,j}}{m_4}\right) \\ &\times \left(1 - 2\frac{\delta m_{2,j}}{m_2} + 3\frac{(\delta m_{2,j})^2}{m_2^2}\right) - 3,\end{aligned} \tag{B5}$$

which after averaging gives

$$\langle \overline{\kappa} \rangle \approx \frac{m_4}{m_2^2}\left(1 + 3\frac{\langle (\delta m_2)^2 \rangle}{m_2^2} - 2\frac{\langle \delta m_2\, \delta m_4 \rangle}{m_2\, m_4}\right) - 3 \neq \kappa. \tag{B6}$$

Thus, averaging the values of the excess kurtosis obtained from runs of finite duration will not lead to the correct value of κ even in the limit of an infinite number of such runs.

A much better procedure is to average the moments over all runs and then use these averaged moments to estimate κ. That is, defining

$$\overline{m_2} = \frac{1}{N}\sum_{j=1}^{N} m_{2,j} \tag{B7}$$

and

$$\overline{m_4} = \frac{1}{N}\sum_{j=1}^{N} m_{4,j}, \tag{B8}$$

we estimate κ as

$$\widetilde{\kappa} = \frac{\overline{m_4}}{(\overline{m_2})^2}. \tag{B9}$$

This is still, strictly speaking, not unbiased; the bias can be estimated using Eq. (B6), with the deviations of the moments replaced by those of their averages ($\delta m_i \to \delta \overline{m_i}$). However, as $\langle (\delta \overline{m_2})^2 \rangle$ and $\langle \delta \overline{m_2}\, \delta \overline{m_4} \rangle$ both decrease as $1/N$ with growing N [see Eqs. (B12) and (B14) below], the bias not only vanishes as $N \to \infty$, but is also negligible compared to the uncertainty of the kurtosis (which goes as $N^{-1/2}$) once N is large enough. Therefore, the estimate (B9) can be considered unbiased and we refer to it as such here and in the main text; it is this estimate that is used to produce the solid symbols in Figs. 6(a), 8, and 11(a). Moreover, even when binning the data to produce the gray curves for individual runs in that plot, the same procedure is used to obtain each data point, although in this case the difference compared to using Eq. (B4) is very minor.

The uncertainty of the estimate (B9) can be evaluated approximately by using Eq. (B5) with $N = 1$, $m_i \to \overline{m_i}$, and $\delta m_i \to \delta \overline{m_i}$. This gives, to first order,

$$\delta \widetilde{\kappa} \approx (\widetilde{\kappa} + 3)\left(\frac{\delta \overline{m_4}}{\overline{m_4}} - 2\frac{\delta \overline{m_2}}{\overline{m_2}}\right), \tag{B10}$$

and then

$$\langle \delta \widetilde{\kappa}^2 \rangle \approx (\widetilde{\kappa} + 3)^2\left(\frac{\langle (\delta \overline{m_4})^2 \rangle}{\overline{m_4}^2} + 4\frac{\langle (\delta \overline{m_2})^2 \rangle}{\overline{m_2}^2} - 4\frac{\langle \delta \overline{m_2}\, \delta \overline{m_4} \rangle}{\overline{m_2}\, \overline{m_4}}\right). \tag{B11}$$

The square root of the last expression, where the uncertainties of the averages are estimated as

$$\langle (\delta \overline{m_2})^2 \rangle \approx \frac{1}{N(N-1)}\sum_{j=1}^{N} (m_{2,j} - \overline{m_2})^2, \tag{B12}$$

$$\langle (\delta \overline{m_4})^2 \rangle \approx \frac{1}{N(N-1)}\sum_{j=1}^{N} (m_{4,j} - \overline{m_4})^2, \tag{B13}$$

$$\langle \delta \overline{m_2}\, \delta \overline{m_4} \rangle \approx \frac{1}{N(N-1)}\sum_{j=1}^{N} (m_{2,j} - \overline{m_2})(m_{4,j} - \overline{m_4}), \tag{B14}$$

is plotted as the error bars in Figs. 6(a), 8, and 11(a).

APPENDIX C: CRITICAL TIME INTERVAL

We have seen that for short time intervals Δt, the displacement distribution $P(\Delta z;\Delta t)$ is dominated by the diffusing-diffusivity effect, whereas at longer time intervals, it is dominated by the shape of the potential $U(z)$. In this section, we derive the scale value Δt_c that divides the two regimes. The basic idea is to balance the diffusion and drift terms in Eq. (5). That is, we want

$$v_d^{(0)}\,\Delta t_c \approx \sqrt{2D_\perp^{(0)}\Delta t_c}, \quad \Rightarrow \quad \Delta t_c \approx \frac{2D_\perp^{(0)}}{\left[v_d^{(0)}\right]^2}, \tag{C1}$$

where $v_d^{(0)}$ is, crudely speaking, the average or typical *absolute value* of the drift velocity and, similarly, $D_\perp^{(0)}$ is the typical value of the vertical diffusivity.

Our first task is to find the most probable distance z_0 between bead and wall, which we do from the minimum of the potential, $U'(z_0)=0$. Using Eq. (4), we have, with $\bar{U}$ denoting energies in units of k_BT,

$$\bar{U}'(z) = -\frac{\bar{B}}{\ell_D}\,e^{-z/\ell_D} + \frac{1}{\ell_g} = 0, \tag{C2}$$

which implies

$$z_0 = \ell_D \ln\left(\bar{B}\,\frac{\ell_g}{\ell_D}\right). \tag{C3}$$

The next task is to estimate the typical force exerted by the potential as the particle fluctuates about the minimum at z_0. We do so by approximating the motion about the minimum z_0 as a harmonic trap with "spring constant" $k = U''(z_0)$, given by

$$\bar{U}''(z_0) = +\frac{\bar{B}}{\ell_D^2}\,e^{-z_0/\ell_D} = \frac{1}{\ell_g\,\ell_D}. \tag{C4}$$

The equipartition theorem then implies a typical displacement

$$\delta z = \pm\sqrt{\frac{k_BT}{k}} = \pm\frac{1}{\sqrt{\bar{U}''(z_0)}} = \pm\sqrt{\ell_g\,\ell_D} \tag{C5}$$

and a typical force divided by k_BT

$$\bar{U}''(z_0)\,\delta z = \pm\sqrt{\bar{U}''(z_0)} = \pm\frac{1}{\sqrt{\ell_g\,\ell_D}}. \tag{C6}$$

The drift velocity has two contributions:

$$v_d \approx \underbrace{D_\perp{}'(z_0)}_{\text{variable } D} - \underbrace{D_\perp(z_0)\,[\bar{U}''(z_0)\,\delta z]}_{\text{force from potential}}$$

$$\approx \frac{D_0}{a}\left(1 \mp \frac{z_0}{\sqrt{\ell_g\,\ell_D}}\right), \tag{C7}$$

where we have approximated the diffusivity and its derivatives by their values at z_0 and, since the beads stay close to the substrate, $D_\perp(z)\approx D_0(z/a)$ and $D_\perp{}'(z)\approx D_0/a$. For the typical value $v_d^{(0)}$ we then take the average of the two absolute values (with the "+" and "−" signs), and since under our conditions $z_0/(\ell_g\ell_D)^{1/2} > 1$, this gives

$$v_d^{(0)} = \frac{D_0 z_0}{a\sqrt{\ell_g\,\ell_D}}. \tag{C8}$$

Similarly for the diffusivity,

$$D_\perp^{(0)} = [D_\perp(z_0 - [\ell_g\ell_D]^{1/2}) + D_\perp(z_0 + [\ell_g\ell_D]^{1/2})]/2$$
$$\approx D_\perp(z_0) \approx D_0\frac{z_0}{a}. \tag{C9}$$

Finally, we compute the balance between drift and diffusion in this approximation. In dimensionless units,

$$\overline{\Delta t_c} = \Delta t_c\left(\frac{D_0}{\ell_g^2}\right)$$
$$= \left(\frac{D_0}{\ell_g^2}\right)\frac{2D_\perp^{(0)}}{\left[v_d^{(0)}\right]^2} = \frac{2a\ell_D}{z_0\ell_g}$$
$$= \frac{2a}{\ell_g \ln\left(\bar{B}\frac{\ell_g}{\ell_D}\right)} \approx 12. \tag{C10}$$

The last step uses numbers from run 11: $\ell_g = 0.123\ \mu$m, $\ell_D = 0.072\ \mu$m, $\bar{B} = 16.8$, and $a = 2.46\ \mu$m. These numbers imply $z_0 \approx 0.24\ \mu$m and $\delta z \approx 0.094\ \mu$m. The result is quite close to the experimental crossover at $\overline{\Delta t_c} \approx 20$, given all the approximations involved and noting, in particular, that, as Fig. 12 shows, the harmonic approximation is not very accurate already at an energy k_BT over the minimum. Interestingly, the crossover between diffusion and Boltzmann regimes in the MSD plot of Fig. 6(b) occurs at $\overline{\Delta t_c} \approx 13.6$, which is even closer to our estimate here.

It is also interesting to note that the same result [Eq. (C10)] can be obtained in a different way, by considering the time it would take the particle to diffuse over the length of the characteristic interval, from $z_0 - (\ell_g\ell_D)^{1/2}$ to $z_0 + (\ell_g\ell_D)^{1/2}$. Since for most of the time interval Δt_c diffusion dominates over drift, we neglect the drift altogether and then the typical time Δt_c it takes to diffuse the distance $2(\ell_g\ell_D)^{1/2}$ is the solution of

$$2\sqrt{\ell_g\ell_D} \approx \sqrt{2D_\perp(z_0)\Delta t_c}, \tag{C11}$$

which gives Eq. (C10).

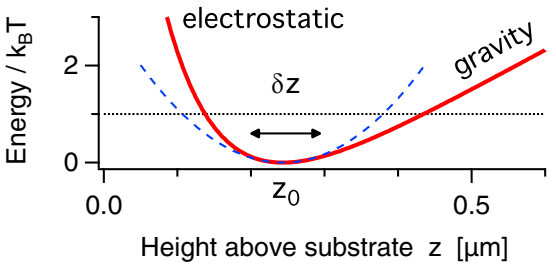

FIG. 12. Particle potential (thick solid curve), generated using parameters from run 11. The potential minimum, at z_0, divides the electrostatic and gravitational regimes. The harmonic approximation is indicated by the dashed curve. The dotted line is k_BT above the minimum. The typical fluctuation scale is of order δz.

[1] A. Einstein, Über die von der molekularkinetischen Theorie der Wärme geforderte Bewegung von in ruhenden Flüssigkeiten suspendierten Teilchen, Ann. Phys. (Leipzig) **322**, 549 (1905).

[2] M. von Smoluchowski, Zur kinetischen Theorie der Brownschen Molekularbewegung und der Suspensionen, Ann. Phys. (Leipzig) **326**, 756 (1906).

[3] C. Gardiner, *Stochastic Methods*, 4th ed. (Springer, Berlin, 2009).

[4] I. Y. Wong, M. L. Gardel, D. R. Reichman, E. R. Weeks, M. T. Valentine, A. R. Bausch, and D. A. Weitz, Anomalous Diffusion Probes Microstructure Dynamics of Entangled F-Actin Networks, Phys. Rev. Lett. **92**, 178101 (2004).

[5] I. M. Tolić-Nørrelykke, E.-L. Munteanu, G. Thon, L. Oddershede, and K. Berg-Sørensen, Anomalous Diffusion in Living Yeast Cells, Phys. Rev. Lett. **93**, 078102 (2004).

[6] J.-H. Jeon, H. Martinez-Seara Monne, M. Javanainen, and R. Metzler, Anomalous Diffusion of Phospholipids and Cholesterols in a Lipid Bilayer and Its Origins, Phys. Rev. Lett. **109**, 188103 (2012).

[7] M. Weiss, M. Elsner, F. Kartberg, and T. Nilsson, Anomalous subdiffusion is a measure for cytoplasmic crowding in living cells, Biophys. J. **87**, 3518 (2004).

[8] I. Golding and E. C. Cox, Physical Nature of Bacterial Cytoplasm, Phys. Rev. Lett. **96**, 098102 (2006).

[9] D. Ernst, J. Köhler, and M. Weiss, Probing the type of anomalous diffusion with single-particle tracking, Phys. Chem. Chem. Phys. **16**, 7686 (2014).

[10] F. Höfling and T. Franosch, Anomalous transport in the crowded world of biological cells, Rep. Prog. Phys. **76**, 046602 (2013).

[11] M. J. Skaug, J. Mabry, and D. K. Schwartz, Intermittent Molecular Hopping at the Solid-Liquid Interface, Phys. Rev. Lett. **110**, 256101 (2013).

[12] B. Wang, S. M. Anthony, S. C. Bae, and S. Granick, Anomalous yet Brownian, Proc. Natl. Acad. Sci. USA **106**, 15160 (2009).

[13] B. Wang, J. Kuo, C. Bae, and S. Granick, When Brownian diffusion is not Gaussian, Nat. Mater. **11**, 481 (2012).

[14] S. Bhattacharya, D. K. Sharma, S. Saurabh, S. De, A. Sain, A. Nandi, and A. Chowdhury, Plasticization of poly(vinylpyrrolidone) thin films under ambient humidity: Insight from single-molecule tracer diffusion dynamics, J. Phys. Chem. B **117**, 7771 (2013).

[15] D. S. Banks, C. Tressler, R. D. Peters, F. Höfling, and C. Fradin, Characterizing anomalous diffusion in crowded polymer solutions and gels over five decades in time with variable-lengthscale fluorescence correlation spectroscopy, Soft Matter **12**, 4190 (2016).

[16] C. Xue, X. Zheng, K. Chen, Y. Tian, and G. Hu, Probing non-Gaussianity in confined diffusion of nanoparticles, J. Phys. Chem. Lett. **7**, 514 (2016).

[17] H. Kai, F. B. Khorasani, S. T. Retterer, D. K. Thomas, J. C. Conrad, and R. Krishnamoorti, Diffusive dynamics of nanoparticles in arrays of nanoposts, ACS Nano **7**, 5122 (2013).

[18] K. C. Leptos, J. S. Guasto, J. P. Gollub, A. I. Pesci, and R. E. Goldstein, Dynamics of Enhanced Tracer Diffusion in Suspensions of Swimming Eukaryotic Microorganisms, Phys. Rev. Lett. **103**, 198103 (2009).

[19] H. Kurtuldu, J. S. Guasto, K. A. Johnson, and J. P. Gollub, Enhancement of biomixing by swimming algal cells in two-dimensional films, Proc. Natl. Acad. Sci. USA **108**, 10391 (2011).

[20] W. K. Kegel and A. van Blaaderen, Direct observation of dynamical heterogeneities in colloidal hard-sphere suspensions, Science **287**, 290 (2000).

[21] E. R. Weeks, J. C. Crocker, A. C. Levitt, A. Schofield, and D. A. Weitz, Three-dimensional direct imaging of structural relaxation near the colloidal glass transition, Science **287**, 627 (2000).

[22] J. Guan, B. Wang, and S. Granick, Even hard-sphere colloidal suspensions display Fickian yet non-Gaussian diffusion, ACS Nano **8**, 3331 (2014).

[23] J. Kim, C. Kim, and B. J. Sung, Simulation Study of Seemingly Fickian but Heterogeneous Dynamics of Two Dimensional Colloids, Phys. Rev. Lett. **110**, 047801 (2013).

[24] H. Jeon, H. W. Cho, J. Kim, and B. J. Sung, Non-Gaussian rotational diffusion in heterogeneous media, Phys. Rev. E **90**, 042105 (2014).

[25] M. V. Chubynsky and G. W. Slater, Diffusing Diffusivity: A Model for Anomalous, yet Brownian, Diffusion, Phys. Rev. Lett. **113**, 098302 (2014).

[26] J. Wang, Y. Zhang, and H. Zhao, Non-Gaussian normal diffusion induced by delocalization, Phys. Rev. E **93**, 032144 (2016).

[27] R. Jain and K. L. Sebastian, Diffusion in a crowded, rearranging environment, J. Phys. Chem. B **120**, 3988 (2016).

[28] R. Jain and K. L. Sebastian, Diffusing diffusivity: Survival in a crowded, rearranging and bounded domain, J. Phys. Chem. B **120**, 9215 (2016).

[29] A. G. Cherstvy and R. Metzler, Anomalous diffusion in time-fluctuating non-stationary diffusivity landscapes, Phys. Chem. Chem. Phys. **18**, 23840 (2016).

[30] N. Samanta and R. Chakrabarti, Tracer diffusion in a sea of polymers with binding zones: Mobile vs frozen traps, Soft Matter **12**, 8554 (2016).

[31] A. V. Chechkin, F. Seno, R. Metzler, and I. M. Sokolov, Brownian yet Non-Gaussian Diffusion: From Superstatistics to Subordination of Diffusing Diffusivities, Phys. Rev. X **7**, 021002 (2017).

[32] Model 190 Fiber-Lite Halogen Illuminator, Dela-Jenner Industries, Boxborough, MA, USA.

[33] UPlanSApo, NA = 1.2, Olympus Corporation, Shinjuku, Tokyo, Japan.

[34] Bemis Co., Neenah, WI, USA.

[35] Top Gun Static Neutralizer, SIMCO Inc., Hatfield, PA, USA.

[36] Model 406, Newport Corporation, Irvine, CA, USA.

[37] Nano OP-65, controlled by Nano-drive 85, Mad City Labs, Madison, WI, USA.

[38] Model FL3-FW-03S1M-C, Point Grey Research, Richmond, British Columbia, Canada.

[39] National Instruments, Austin, TX, USA.

[40] 2 MHz function generator, Model 3011b, B&K Precision Corporation, Yorba Linda, CA, USA.

[41] M. Goulian and S. M. Simon, Tracking single proteins within cells, Biophys. J. **79**, 2188 (2000).

[42] T. Savin and P. S. Doyle, Static and dynamic errors in particle tracking microrheology, Biophys. J. **88**, 623 (2005).

[43] A. E. Cohen, Trapping and manipulating single Molecules in solution, Ph.D. Thesis, Stanford University, 2006.

[44] A. J. Goldman, A. G. Cox, and H. Brenner, Slow viscous motion of a sphere parallel to a plane wall—I: Motion through a quiescent fluid, Chem. Eng. Sci. **22**, 637 (1967).

[45] J. Happel and H. Brenner, *Low Reynolds Number Hydrodynamics: With Special Applications to Particulate Media* (Springer, Berlin, 1983).

[46] H. Brenner, The slow motion of a sphere through a viscous fluid towards a plane surface, Chem. Eng. Sci. **16**, 242 (1961).

[47] M. A. Bevan and D. C. Prieve, Hindered diffusion of colloidal particles very near to a wall: Revisited, J. Chem. Phys. **113**, 1228 (2000).

[48] L. P. Faucheux and A. J. Libchaber, Confined Brownian motion, Phys. Rev. E **49**, 5158 (1994).

[49] B. Lin, J. Yu, and S. A. Rice, Direct measurements of constrained Brownian motion of an isolated sphere between two walls, Phys. Rev. E **62**, 3909 (2000).

[50] A. Banerjee and K. D. Kihm, Experimental verification of near-wall hindered diffusion for the Brownian motion of nanoparticles using evanescent wave microscopy, Phys. Rev. E **72**, 042101 (2005).

[51] P. Sharma, S. Ghosh, and S. Bhattacharya, A high-precision study of hindered diffusion near a wall, Appl. Phys. Lett. **97**, 104101 (2010).

[52] C. Ha, H. D. Ou-Yang, and H. K. Pak, Direct measurements of colloidal hydrodynamics near flat boundaries using oscillating optical tweezers, Physica A **392**, 3497 (2013).

[53] M. D. Carbajal-Tinoco, R. Lopez-Fernandez, and J. L. Arauz-Lara, Asymmetry in Colloidal Diffusion near a Rigid Wall, Phys. Rev. Lett. **99**, 138303 (2007).

[54] T. G. Van de Ven, *Colloidal Hydrodynamics* (Academic Press, New York, 1989).

[55] M. Yang and M. Ripoll, Brownian motion in inhomogeneous suspensions, Phys. Rev. E **87**, 062110 (2013)

[56] A. W. C. Lau and T. C. Lubensky, State-dependent diffusion: Thermodynamic consistency and its path integral formulation, Phys. Rev. E **76**, 011123 (2007).

[57] P. Lançon, G. Batrouni, L. Lobry, and N. Ostrowsky, Brownian walker in a confined geometry leading to a space-dependent diffusion coefficient, Physica A **304**, 65 (2002).

[58] H. C. Thode, *Testing for Normality* (CRC Press, Boca Raton, FL, 2002).

[59] The uncertainties of these parameters given here and in the main text are statistical and omit comparable systematic uncertainties due, for example, to temperature calibration. The statistical uncertainties are what is relevant when comparing measurements using different beads.

[60] S. Hapca, J. W. Crawford, and I. M. Young, Anomalous diffusion of heterogeneous populations characterized by normal diffusion at the individual level, J. R. Soc. Interface **6**, 111 (2009).

[61] I. H. Riedel, K. Kruse, and J. Howard, A self-organized vortex array of hydrodynamically entrained sperm cells, Science **309**, 300 (2005)

[62] A. Sokolov, I. S. Aranson, J. O. Kessler, and R. E. Goldstein, Concentration Dependence of the Collective Dynamics of Swimming Bacteria, Phys. Rev. Lett. **98**, 158102 (2007).

[63] M. Matse, State-dependent diffusion of Brownian particles near a boundary wall, M.Sc. thesis, Simon Fraser University, 2015.